AD-A278 629

||||||||||||||

An Efficient, Intelligent Solution for Viscous Flows Inside Solid Rocket Motors

November 1993

Prepared by

I-SHIH CHANG
Engineering and Technology Group

Prepared for

SPACE AND MISSILE SYSTEMS CENTER
AIR FORCE MATERIEL COMMAND
2430 E. El Segundo Boulevard
Los Angeles Air Force Base, CA 90245

DTIC
ELECTE
APR 2 6 1994
S B D

Programs Group

DTIC QUALITY INSPECTED 3

94-12673

|||||||||||||||||||||

THE AEROSPACE CORPORATION

94 4 25 085

Douglas A. Van Mullem

REPORT DOCUMENTATION PAGE

Form Approved
OMB No. 0704-0188

1. AGENCY USE ONLY (Leave blank)	2. REPORT DATE	3. REPORT TYPE AND DATES COVERED
	November 1993	TR/Jan. 1990 to Jan. 1991

4. TITLE AND SUBTITLE

An Efficient, Intelligent Solution for Viscous Flows Inside Solid Rocket Motors

5. FUNDING NUMBERS

6. AUTHOR(S)

I-Shih Chang

7. PERFORMING ORGANIZATION NAME(S) AND ADDRESS(ES)

The Aerospace Corporation
2350 E. El Segundo Blvd.
El Segundo, CA 90245-4691

8. PERFORMING ORGANIZATION REPORT NUMBER

TR-93(3530)-3

9. SPONSORING/MONITORING AGENCY NAME(S) AND ADDRESS(ES)

Space and Missile Systems Center
Air Force Materiel Command
2430 E. El Segundo Blvd.
Los Angeles Air Force Base, CA 90245

10. SPONSORING/MONITORING AGENCY REPORT NUMBER

SMC-TR-94-25

11. SUPPLEMENTARY NOTES

12a. DISTRIBUTION/AVAILABILITY STATEMENT

Approved for public release; distribution unlimited

12b. DISTRIBUTION CODE

13. ABSTRACT (Maximum 200 words)

An efficient, intelligent method has been developed for the solution of axisymmetric, compressible viscous flows inside solid rocket motors. The method applies an adaptive, unstructured, finite-element mesh generation technique and a cell-centered, second-order, flux correction transport scheme for the solution of Navier-Stokes equations. With known, initial motor interior configuration, the method developed in this study allows the computational boundaries to be determined intelligently, the finite-element meshes and remeshes to be generated efficiently, and the corresponding compressible viscous flow fields to be produced expeditiously. Very good agreement between analysis results and test data is obtained for flow inside the Jet Propulsion Laboratory nozzle. Application of the method to analyze flows inside the Titan IV solid rocket motor upgrade and the Star-48 motor with very complicated chamber and nozzle geometry is illustrated.

DTIC QUALITY INSPECTED 3

14. SUBJECT TERMS
Viscous Flow, Solid Rocket Motor, Finite-Element Analysis

15. NUMBER OF PAGES
31

16. PRICE CODE

17. SECURITY CLASSIFICATION OF REPORT	18. SECURITY CLASSIFICATION OF THIS PAGE	19. SECURITY CLASSIFICATION OF ABSTRACT	20. LIMITATION OF ABSTRACT
Unclassified	Unclassified	Unclassified	Unlimited

CONTENTS

FIGURES

1. INTRODUCTION

In many instances, the engineering staff is requested by program planning personnel to provide answers to a certain design question regarding a launch vehicle, which is in the development/qualification stage, or to abnormal behavior of a vehicle in flight. Often, a quick response is important, in order that pertinent decisions can be made which have major impact on cost and scheduling of a program. This kind of request is common in the area concerning flows inside solid rocket motors. Existing techniques for motor internal flow analysis usually require time-consuming and extensive labor for geometry modeling and flow-field solution and cannot provide analysis results in an expeditious, satisfactory manner.

In this study, an efficient, intelligent method for the solution of compressible viscous flows inside solid rocket motors is developed to provide timely analysis support of launch vehicle design, qualification, and flight hardware evaluation for the Air Force Space and Missile Systems Center. The method applies an adaptive, unstructured, finite-element mesh generation technique and a cell-centered, second-order, flux correction transport scheme for the solution of Navier-Stokes equations, which include every term in the viscous stress tensor. The method, originally developed at the University of Wales, Swansea, England (Ref. 1), and NASA Langley Research Center and contractors (Refs. 2 and 3) for the study of a plane two-dimensional, supersonic flow over a circular cylinder, is extended and streamlined to the solution of axisymmetric flows inside solid rocket motors of arbitrary configuration with a nonuniform inlet boundary condition.

With known, initial motor interior configuration, the program developed in this study allows the computational boundaries—including propellant burn-backs, ablated motor case insulation, and eroded nozzle-exit cone surface at any time slices after ignition—to be determined intelligently. The basic meshes and corresponding compressible viscous flow fields then are generated for the specified computational boundaries. Based on the results of flow analyses on the basic meshes, the element sizes are refined in high-gradient regions and unrefined in low-gradient regions. The remeshes, thus obtained, are appropriate for cost-effective production flow-field runs. The process of calculation is fully automated, resulting in smooth flow in transmitting computational results from one module to another.

The advantages of using the present method are as follows:

- Easy implementation of an exact design configuration
- Optimum use of computational resources
- High resolution analysis results for minimum cost
- Elimination of elapsed time through an automated procedure
- Same procedure for any complicated configuration
- Same mesh generation program for different applications, such as thermal and structural analyses
- Significant reduction in effort required for a complete solid rocket motor internal flow-field solution

It can be said that because of its flexibility and versatility in treating complicated geometry in multidimensional space, the adaptive, unstructured finite-element method for the solution of Navier-Stokes equations will be the main computational technique for flow analysis in the coming decade. In the following sections, the formulation and the solution method will be discussed. Application of the method to the solution of axisymmetric compressible viscous

flows inside the Jet Propulsion Laboratory (JPL) nozzle, the Titan IV solid rocket motor upgrade (SRMU) nozzle, and the Star-48 motor with a very complicated chamber and nozzle geometry will be illustrated.

2. FORMULATION

The Navier-Stokes equations in cylindrical coordinates for a plane two-dimensional or an axisymmetric space are:

$$\frac{\partial D}{\partial t} = \frac{\partial E_x}{\partial x} + \frac{1}{r^\delta}\frac{\partial\left(r^\delta E_r\right)}{\partial r} + \frac{\delta}{r}F \tag{1}$$

$$D = \begin{bmatrix} \varrho \\ \varrho u \\ \varrho v \\ \varrho e \end{bmatrix}$$

$$E_x = \begin{bmatrix} 0 \\ \tau_{xx} \\ \tau_{rx} \\ u\tau_{xx} + v\tau_{rx} + K\dfrac{\partial T}{\partial x} \end{bmatrix} - \begin{bmatrix} \varrho u \\ p + \varrho u^2 \\ \varrho uv \\ u(p + \varrho e) \end{bmatrix}$$

$$E_r = \begin{bmatrix} 0 \\ \tau_{rx} \\ \tau_{rr} \\ v\tau_{rr} + u\tau_{rx} + K\dfrac{\partial T}{\partial r} \end{bmatrix} - \begin{bmatrix} \varrho v \\ \varrho uv \\ p + \varrho v^2 \\ v(p + \varrho e) \end{bmatrix}$$

$$F = \begin{bmatrix} 0 \\ 0 \\ -\tau_{\theta\theta} \\ 0 \end{bmatrix} - \begin{bmatrix} 0 \\ 0 \\ -p \\ 0 \end{bmatrix}$$

where $\delta = 0$ or 1, depending on the configuration

$$\begin{cases} \tau_{rr} = -\dfrac{2}{3}\mu\,\nabla\cdot\hat{v} + 2\mu\dfrac{\partial v}{\partial r} \\[2mm] \tau_{xx} = -\dfrac{2}{3}\mu\,\nabla\cdot\hat{v} + 2\mu\dfrac{\partial u}{\partial x} \\[2mm] \tau_{\theta\theta} = -\dfrac{2}{3}\mu\,\nabla\cdot\hat{v} + 2\mu\dfrac{v}{r} \\[2mm] \tau_{rx} = \tau_{xr} = \mu\left(\dfrac{\partial u}{\partial r} + \dfrac{\partial v}{\partial x}\right) \end{cases}$$

and

$$\nabla\cdot\hat{v} = \frac{\partial v}{\partial r} + \frac{\delta v}{r} + \frac{\partial u}{\partial x}$$

7

Sutherland's theory of viscosity for air is

$$\frac{\mu}{\mu_o} = \left(\frac{T}{T_o}\right)^{3/2} \frac{T_o + S_1}{T + S_1}$$

where $T_o = 492°R$, $S_1 = 199°R$, and $\mu_o = 2.4865 \times 10^{-9}$ lb$_f$ – sec/in.^{2}.

The power law for viscosity of combustion gas is

$$\frac{\mu}{\mu_{ref}} = \left(\frac{T}{T_{ref}}\right)^A$$

where A = constant for a combustion gas.

Multiplied by a differential area $(2\pi r)^\delta$ drdx, and integrated over an element, with the application of divergence theorem on the first two terms of the right-hand side, Eq. (1) becomes

$$\frac{\Delta D_e}{\Delta t} = \frac{1}{\Omega_e \, r_e^\delta} \int_\Gamma E_n r^\delta ds + \frac{\delta}{r_e} Fe \tag{2}$$

where

Ω_e = area of element

r_e = radial coordinate of element centroid

Γ = boundary of element

E_n = flux normal to the boundary of element

e = subscript indicates flow variable at element centroid

3. SOLUTION METHOD

Notice that in Eq. (2), $\delta = 0$ is for a plane two-dimensional configuration, and $\delta = 1$ is for an axisymmetric configuration. When governing equations are written in the form shown in Eq. (2), the second-order, flux correction transport scheme for solution of the plane two-dimensional Navier-Stokes equations, contained in the computer program LARC/NESS (Langley Adaptive Remeshing Code and Navier-Stokes Solver) and developed in References 1 through 3, can be modified easily and adopted to axisymmetric configurations by including the terms required for axisymmetry. The detailed solution method based on this scheme is discussed in Reference 2.

For rocket nozzle flows, the initial condition for this time-dependent scheme is derived from a one-dimensional isentropic assumption. The exit boundary condition is based on a simple linear extrapolation, since the flow is assumed to be supersonic at the exit plane, and the error generated from the extrapolation is not expected to propagate back and affect the upstream results. There are several different schemes (e.g., Refs. 4 and 5) for implementing an inlet boundary condition in a time-dependent nozzle flow calculation. The characteristics formulation shown in Reference 4 and used in Reference 6 provides a fairly smooth subsonic flow in the physical domain and is applied here in an adaptive, unstructured mesh form, if the inlet boundary is not on the propellant burning surface. When the inlet boundary lies on the propellant burning surface, the flow variables on the inlet boundary are determined from propellant burn-rate, chamber temperature, and pressure.

For a viscous flow, the nozzle wall is a non-slip boundary with a specified wall temperature. For an inviscid flow, the nozzle wall is a slip boundary with the velocity vector tangent to the wall surface. For a cell-centered scheme, such as the one used in this study, the radius of element centroid is always a finite value and never becomes zero. Therefore, no singularity problem is associated with the calculation of flow variables at the elements containing the centerline as one of the element boundaries in the present cell-centered formulation. The flux across the centerline boundary is zero. For other finite-element methods with a node-centered scheme, Reference 7 provides a technique for resolving the numerical difficulty encountered at the singular centerline. From numerical experimentation, it is advisable to use a smaller integration step size in an axisymmetric space than that in a plane two-dimensional space.

The plane two-dimensional LARC/NESS program (Ref. 2) has been enhanced for an axisymmetric calculation in this study through the following:

- Developing an auxiliary program for intelligently determining computational boundaries that include propellant burn-backs, ablated motor case insulation, and eroded nozzle-exit cone surface at any time slice after ignition

- Streamlining the program to automatically blend a structured mesh in the boundary layer with an unstructured mesh in the main flow region for any arbitrary geometry

- Employing an isentropic initial guess to start a nozzle flow calculation on an unstructured mesh

- Implementing procedures for evaluating nonuniform inlet boundary conditions

- Including every term in the governing Eq. (1) for an axisymmetric configuration

- Incorporating a power law, viscosity-temperature relationship for combustion gas, in addition to Sutherland's theory of viscosity for air

9

- Simplifying the meshing and remeshing procedure through automated data transmissions between the different computational modules
- Utilizing publication-quality plotting routines for post-processing data displays

4. THE JPL NOZZLE

The flow inside the JPL axisymmetric convergent-divergent nozzle (Ref. 8) with a 45° entrance and a 15° exit straight wall tangent to a circular throat (with ratio of throat radius of curvature to throat height = 0.625) provides a classic comparison for transonic nozzle flow analysis. The cold flow test was conducted with air at a stagnation pressure of 70 psia and a stagnation temperature of 540°R.

Figure 1 shows the basic mesh and remesh for the JPL nozzle flow calculation. The remesh was obtained after 500 integration steps on the basic mesh. There are 20 stretched, structured elements (with the first element height 10^{-4} in.) covering the thickness of the viscous layer, which envelops the nozzle wall boundary. The total number of elements is 3298 (1140 structured quadrilateral + 2158 unstructured triangular elements) for the basic mesh and 2328 (1280 structured quadrilateral + 1048 unstructured triangular elements) for the remesh.

BASIC MESH
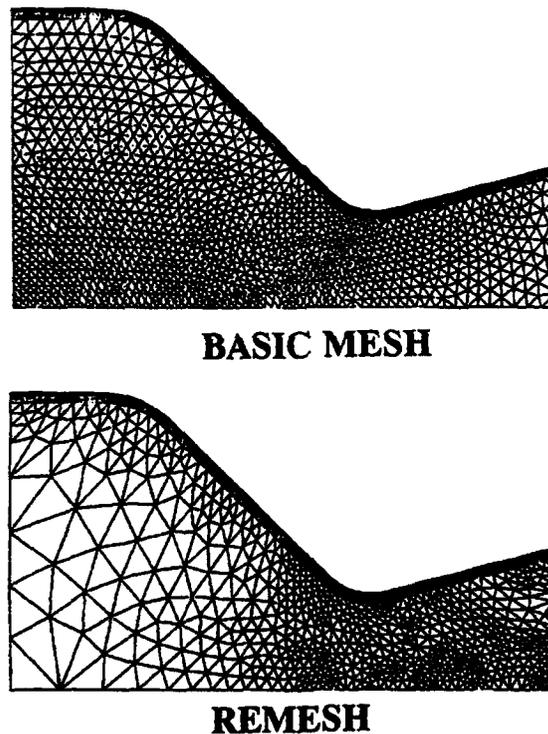
REMESH

Figure 1. JPL Nozzle Meshes

Sutherland's theory of viscosity for air is employed in the JPL nozzle flow calculation. The computed dimensionless pressure ratio (P/Po) and Mach number contours are shown in Figure 2. The pressure contour has a constant increment of 0.025, and the Mach number contour has a constant increment of 0.1. The flow recompression near the wall downstream of the throat, which was observed in a cold flow test (Ref. 8), can be seen from the contour plots. The enlarged view of the remesh and Mach number contours in the throat region is depicted in Figure 3, where the structured mesh near the wall blending with the unstructured mesh for the main flow is distinguishable. The calculated boundary layer thickness shown in Figure 3 is less than that observed in Reference 8, mainly because of the laminar flow assumption in the present study.
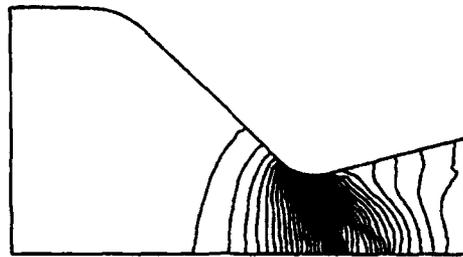
PRESSURE CONTOUR
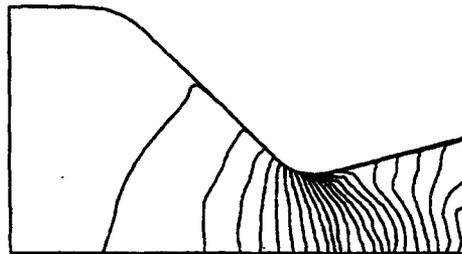
MACH NUMBER CONTOUR

Figure 2. JPL Nozzle Pressure and Mach Number
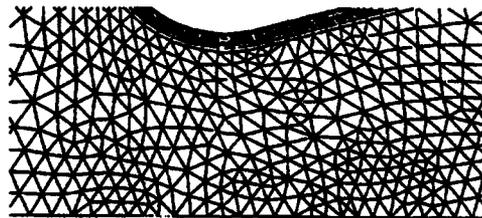
REMESH
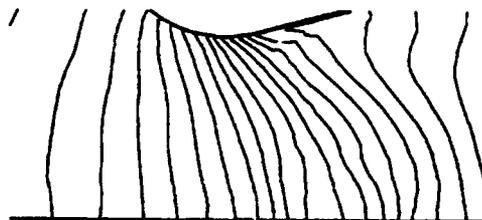
MACH NUMBER CONTOUR

Figure 3. JPL Nozzle Throat Region

The computed pressure and Mach number distributions along the wall and centerline are illustrated in Figures 4 and 5. Shown in the same figures for comparison are nozzle wall geometry and test data from Reference 8. The computed results agree very well with test data in the entire subsonic-transonic-supersonic flow regime. This indicates that the boundary conditions are implemented correctly for the axisymmetric nozzle flow calculation with an adaptive, unstructured mesh and assures further application of the computer program to other nozzle configurations. In general, the present viscous analysis results show similar flow features to those presented in Reference 6. A somewhat better flow resolution is obtained from the present analysis than that of the inviscid flow analysis of Reference 6 in the low-speed compression corner area, where the viscous effect prevails.
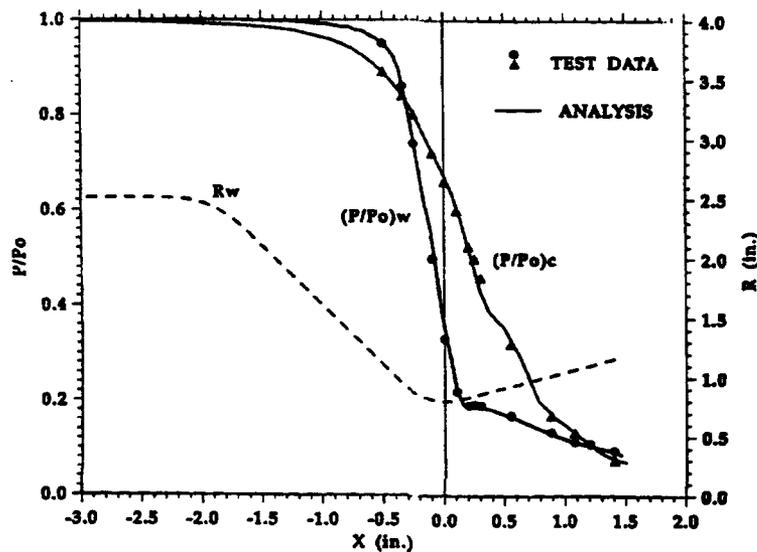
Figure 4. JPL Nozzle Pressure Distribution
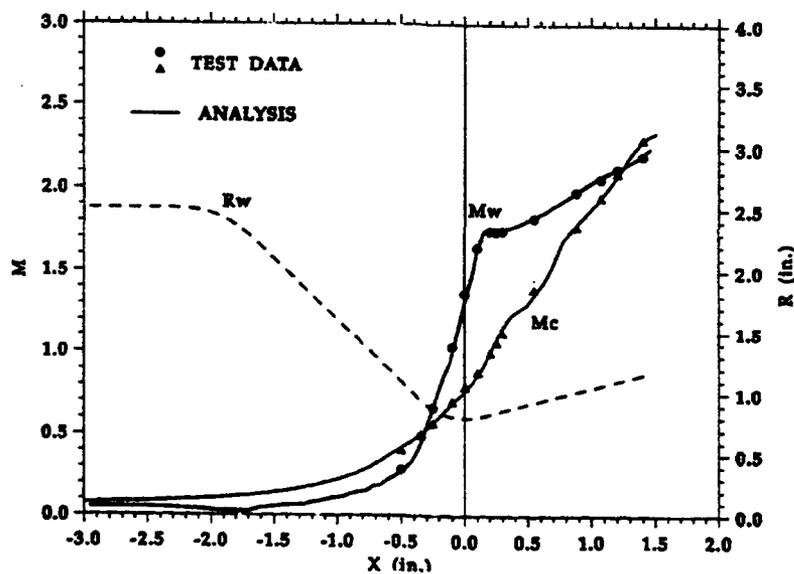
Figure 5. JPL Nozzle Mach Number Distribution

13

No test data are available for comparison with the computed convective heating rate shown in Figure 6. In the present calculation, the nozzle wall temperature is held constant at $500°R$. The analysis indicates that gas pressure stays essentially unchanged until it approaches the throat. The highest positive (gas to wall) heating rate in Figure 6 is indicative of high gas energy recovery near the wall at a high contraction ratio location. As flow passes through the throat, the gas pressure decreases rapidly and the gas temperature falls below the constant value at the wall, and a negative (wall to gas) heating rate occurs. The absolute value of a computed heat exchange between the gas and the nozzle wall for laminar flow has a peak at the throat, which also is observed from the turbulent flow heating rate measurement carried out in Reference 9 for a convergent-divergent nozzle flow. The energy equation in Eq. (2) converges much slower than the continuity and momentum equations. An accurate heating rate calculation requires many integration steps with very fine structured elements in a viscous layer. This is an area which needs to be improved in the future.
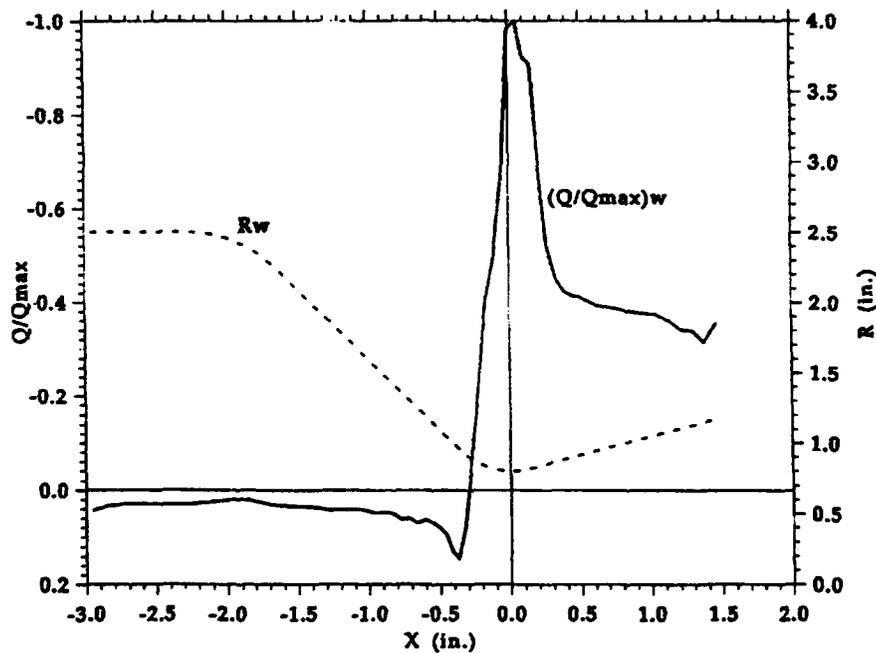
Figure 6. JPL Nozzle Wall Heating Rate

5. THE TITAN IV SRMU

The Air Force Titan IV SRMU (Ref. 10), shown in Figure 7, is being developed to launch large payloads. This is a 126-in. diameter, 112-ft long, three-segment motor with a graphite epoxy composite case (33,600 lb lighter than a steel case). The motor is loaded with 688,850 lb hydroxylterminated polybutadiene (HTPB) propellant (69% ammonium perchlorate + 19% aluminum + 12% binder) and weighs about 772,750 lb. The nozzle throat is made of graphite/phenolic, and the exit cone has a tape-wrapped carbon/phenolic forward insulator and silica/phenolic aft insulator. The nozzle has a composite elastomer flexseal with a maximum 6° gimbal. The maximum mass flow rate is 5700 lb/sec which produces approximately 1.6 million lbf thrust for each SRMU during liftoff. The Titan IV with two SRMUs on each side of the core vehicle is designed to put a 41,000 lb nominal payload into low earth orbit. There will be five full-scale static motor tests during the development and qualification phases.
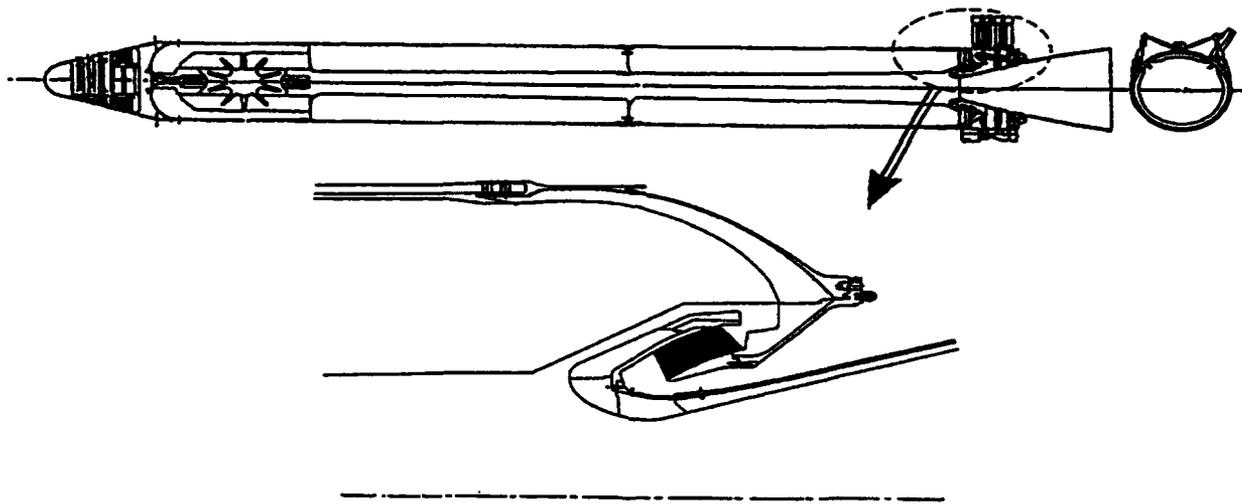
Figure 7. Titan IV SRMU Baseline Design

Ordinarily, a cold flow test would be required to obtain flow-field information for a thermostructural evaluation of nozzle design adequacy. The cold flow test would cost at least one-half million dollars and would require a one-year set-up time for a limited number of propellant burn-backs. The efficient, intelligent method developed in this report for the solution of viscous flows inside solid rocket motors can generate flow solutions for any number of propellant burn-backs within a few days.

The expected motor head-end chamber pressure history is given in Figure 8. Figure 9 shows ablated motor case insulation, eroded nozzle, and propellant burn-backs for the Titan IV SRMU at 0, 25, 50, 75, and 100 sec after ignition. The motor case insulation ablation rate is 5 mil/sec. The erosion rate varies along nozzle-exit cone stations and is projected to be 10 mil/sec at the throat. The propellant burn-rate is a function of pressure ($0.03454 \bullet P^{0.32}$). For the SRMU flow-field calculation, the ratio of specific heats is 1.156, the Prandtl number is 0.57, and the power law viscosity-temperature relationship has an exponent $A = 0.67$ and reference chamber viscosity $1.382 \bullet 10^{-8}$ lbf-sec/in.^{2} at temperature 6364°R.

15
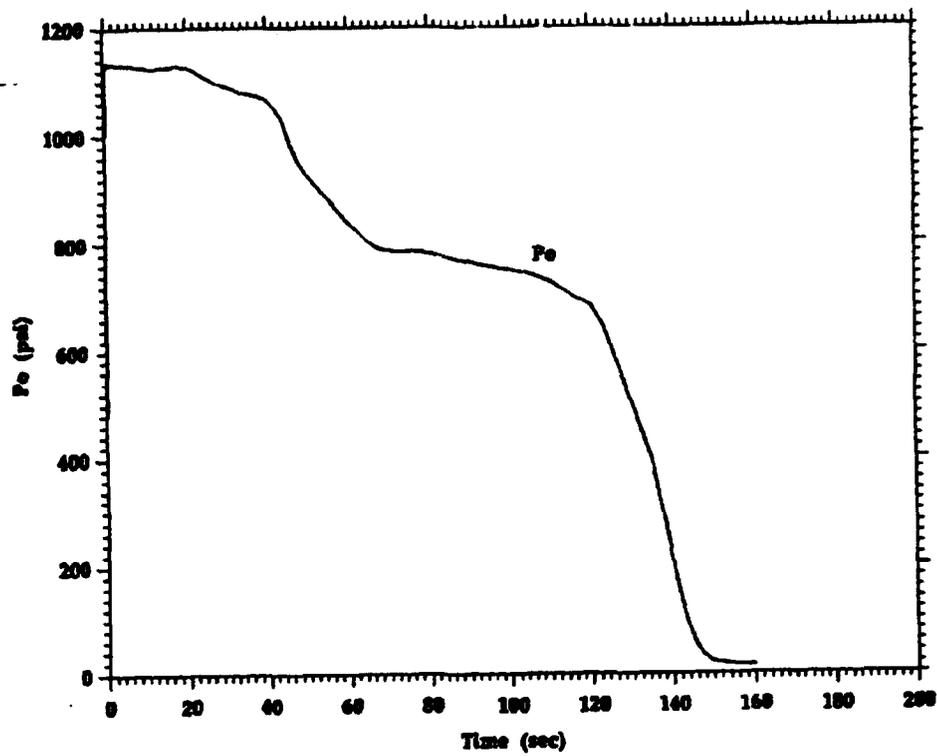
Figure 8. SRMU Chamber Pressure History
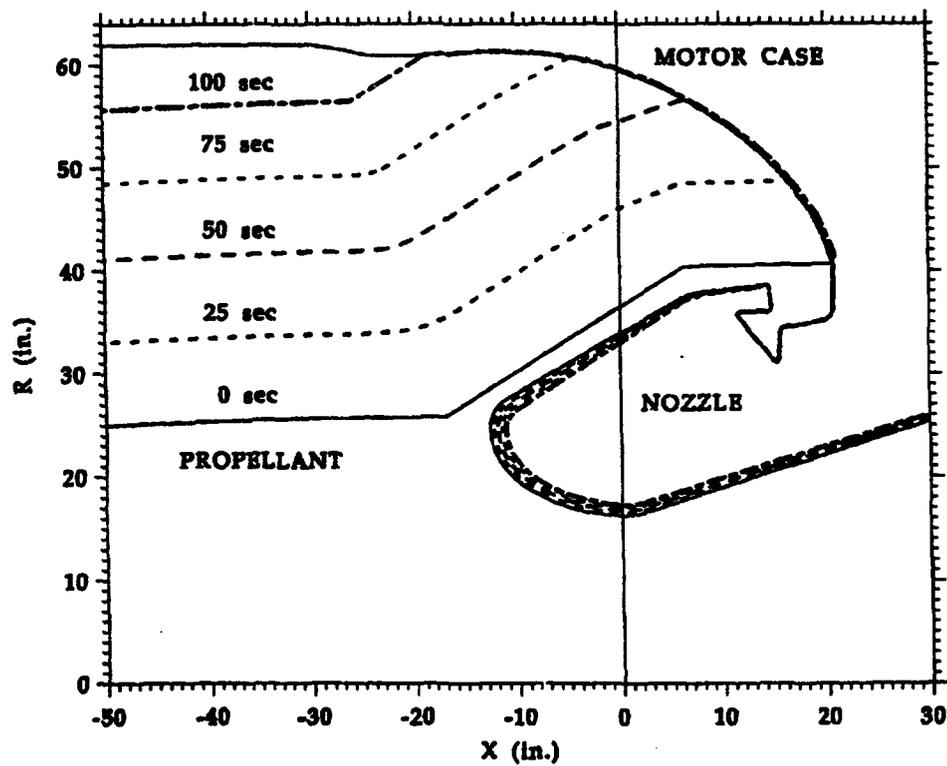
Figure 9. SRMU Nozzle, Motor Case, and Propellant

Figure 10 shows the basic meshes and remeshes at 0, 50, and 100 sec after ignition. The remeshes are obtained after 500 integration steps on the basic meshes. There are 5717, 6321, and 6733 elements for the basic meshes at 0, 50, and 100 sec after ignition. Correspondingly, there are 4442, 5838, and 5950 elements at 0, 50, and 100 sec for the remeshes. These include 20 stretched, structured elements covering the thickness of viscous layer, which envelops the nozzle-exit cone wall. Figure 11 shows the computed Mach numbers and dimensionless pressure ratio (P/Po) contours at 0, 50, and 100 sec after ignition. The enlarged view of the remeshes and Mach number contours in the nozzle region is depicted in Figure 12. The Mach number and pressure distributions on the wall and centerline are given in Figures 13 and 14, respectively. Figures 15 and 16 show the detailed pressure distributions in the nozzle and exit cone regions.

To cover the entire nozzle and the exit cone pressure field, a nonuniform contour increment is used in the Titan IV SRMU pressure contour plots. For a pressure ratio greater than or equal to 0.8, a constant increment of 0.025 is used. For a pressure ratio less than 0.8, a decreasing factor of 0.9 is applied to each subsequent contour value. This covers the pressure field better than that using a linear or a logarithmic contour increment. The Mach number contour, however, can be adequately displayed with a constant increment of 0.1.

The computed ratio of static-to-chamber pressure at the exit plane of the exit cone is 1% at the wall and 0.6% at the centerline. For a viscous analysis, the Mach number at the wall is zero. The "Mw" in Figure 13 representing the gas Mach number at the edge of the boundary layer is evaluated from an isentropic relation at the local wall pressure. The Mach number at the exit plane of the exit cone is 3.3 at the wall and 3.5 at the centerline. There are some differences in the flow field at different times from ignition; these can be observed from the contour plots and Mach number and pressure distributions. It is interesting to note that the pressure remains nearly constant at the chamber pressure condition on the backside of the submerged nozzle and decreases rapidly as gas flows through the throat. This pressure distribution is important for detailed nozzle thermostructural analysis and nozzle design adequacy assessment.

BASIC MESH

REMESH

0 sec

0 sec

50 sec

50 sec

100 sec

100 sec

Figure 10. SRMU Meshes

MACH NUMBER

PRESSURE

0 sec

0 sec

50 sec

50 sec

100 sec

100 sec
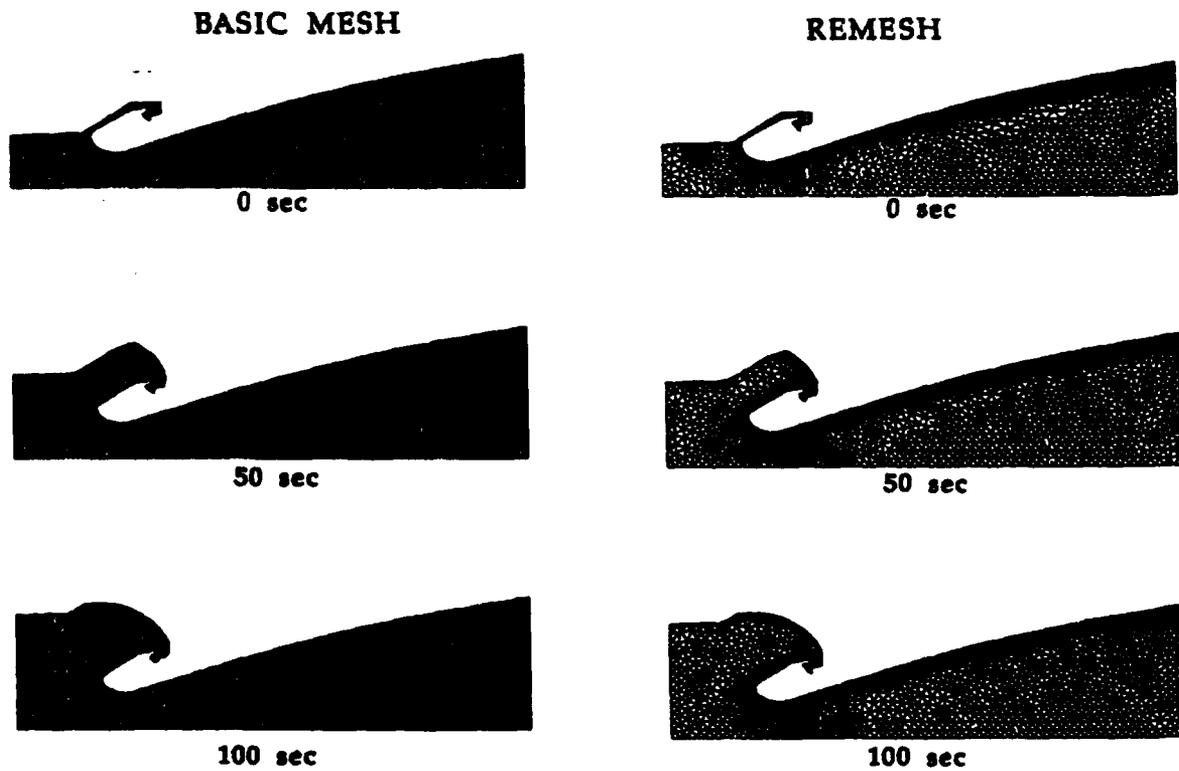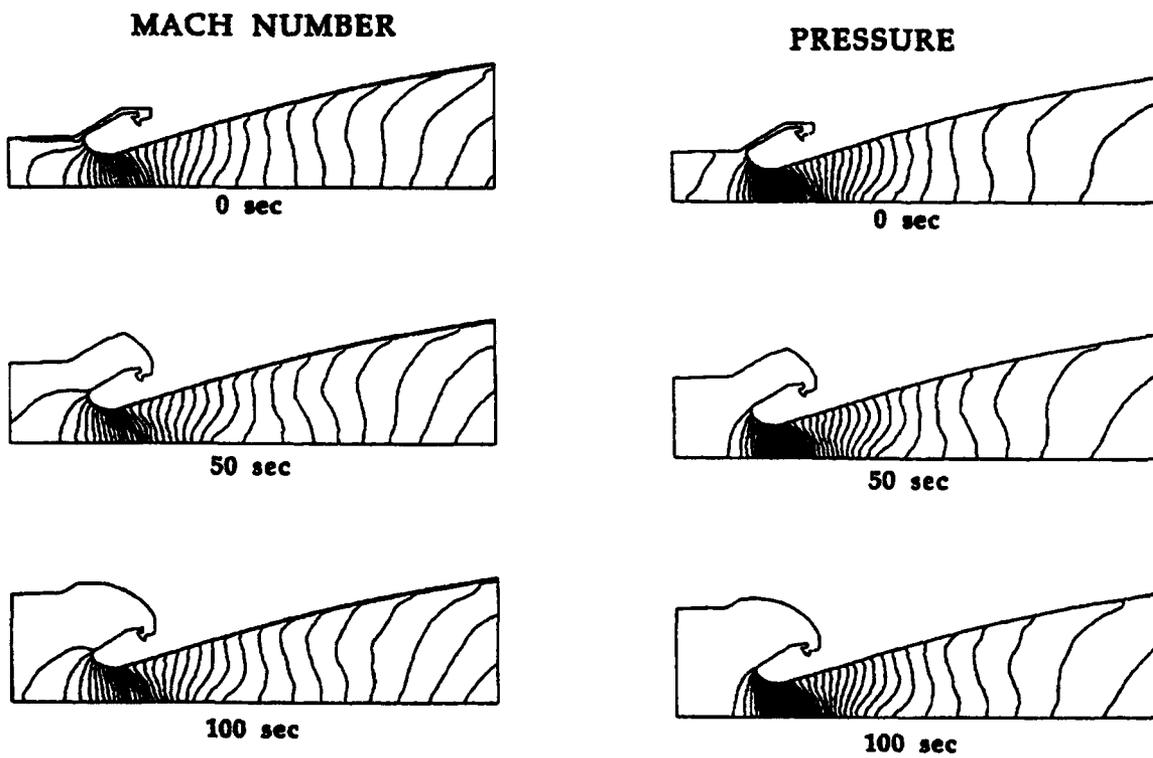
Figure 11. SRMU Pressure and Mach Number

REMESH   MACH NUMBER

0 sec

50 sec

100 sec
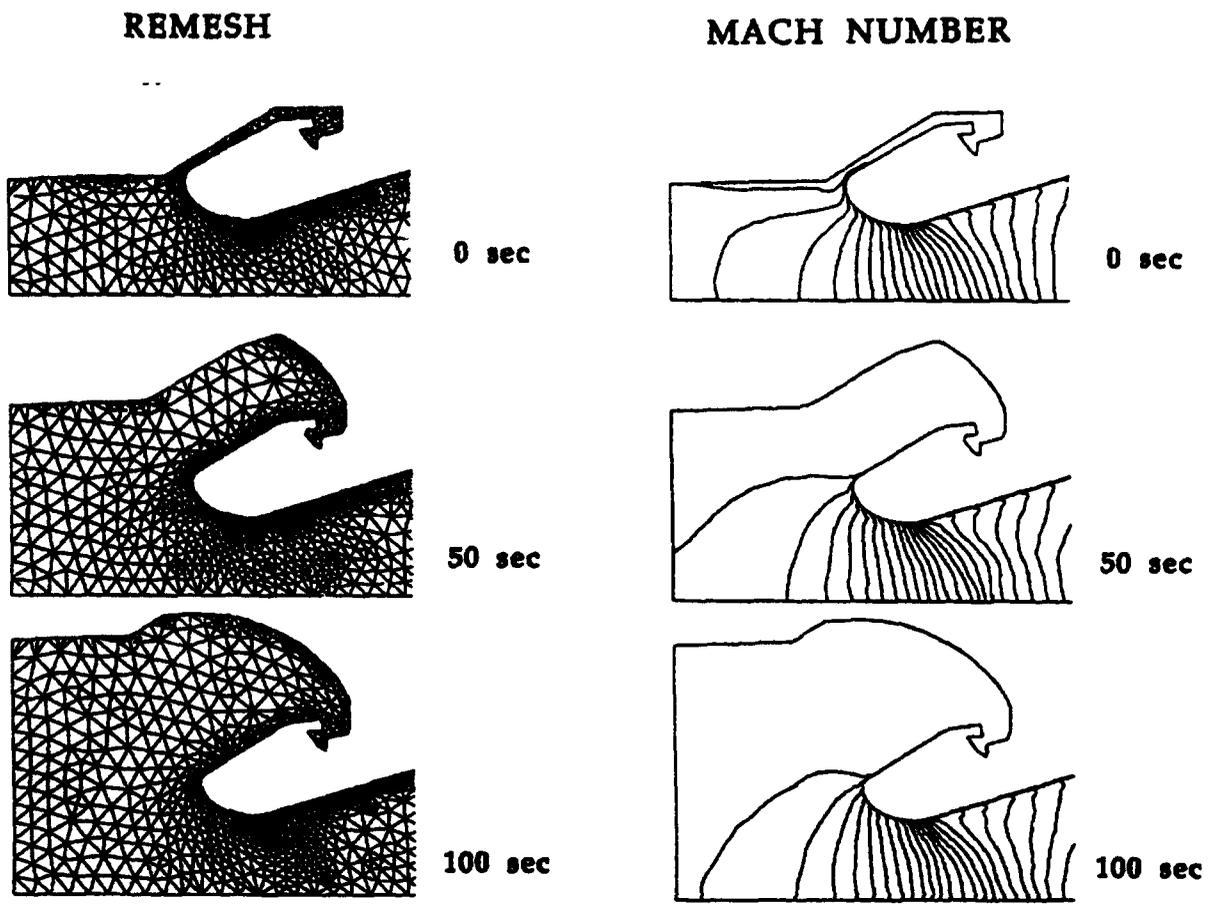
Figure 12. SRMU Nozzle Region
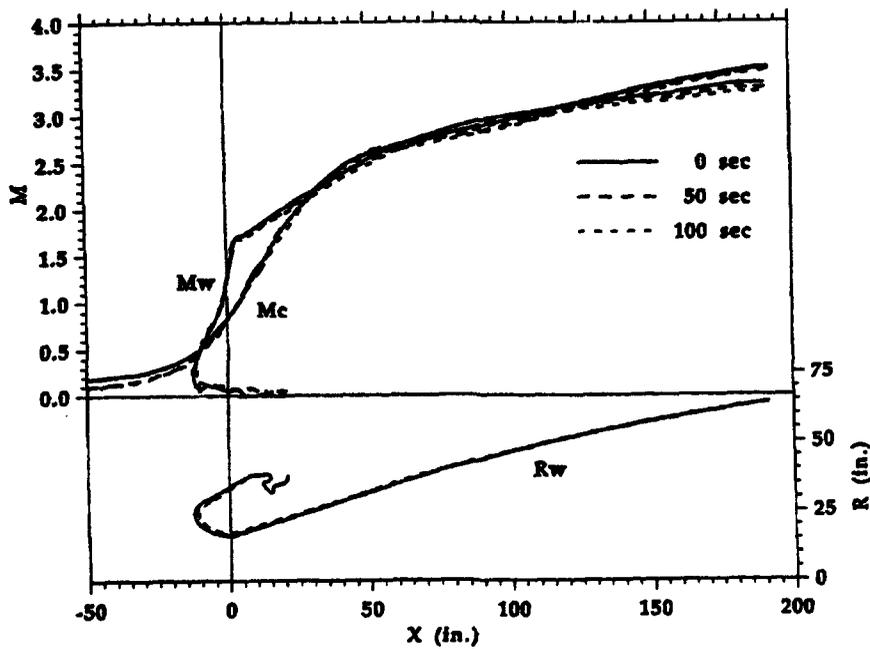
Figure 13. SRMU Mach Number Distribution

19
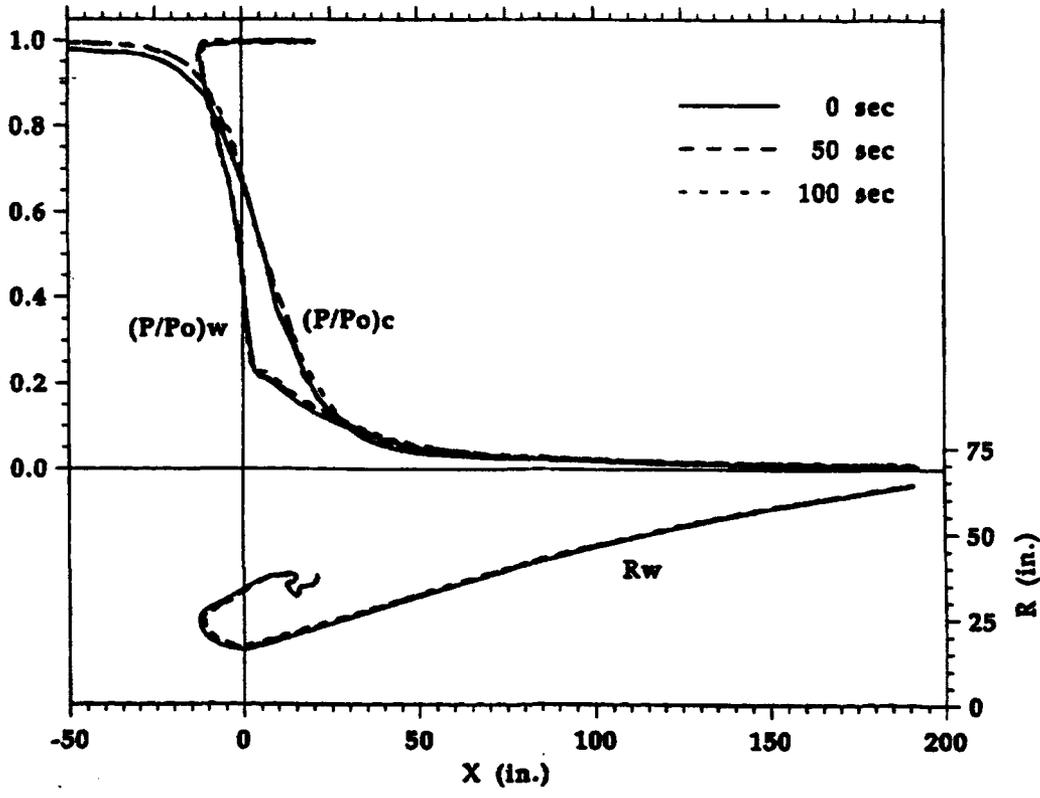
Figure 14. SRMU Pressure Distribution
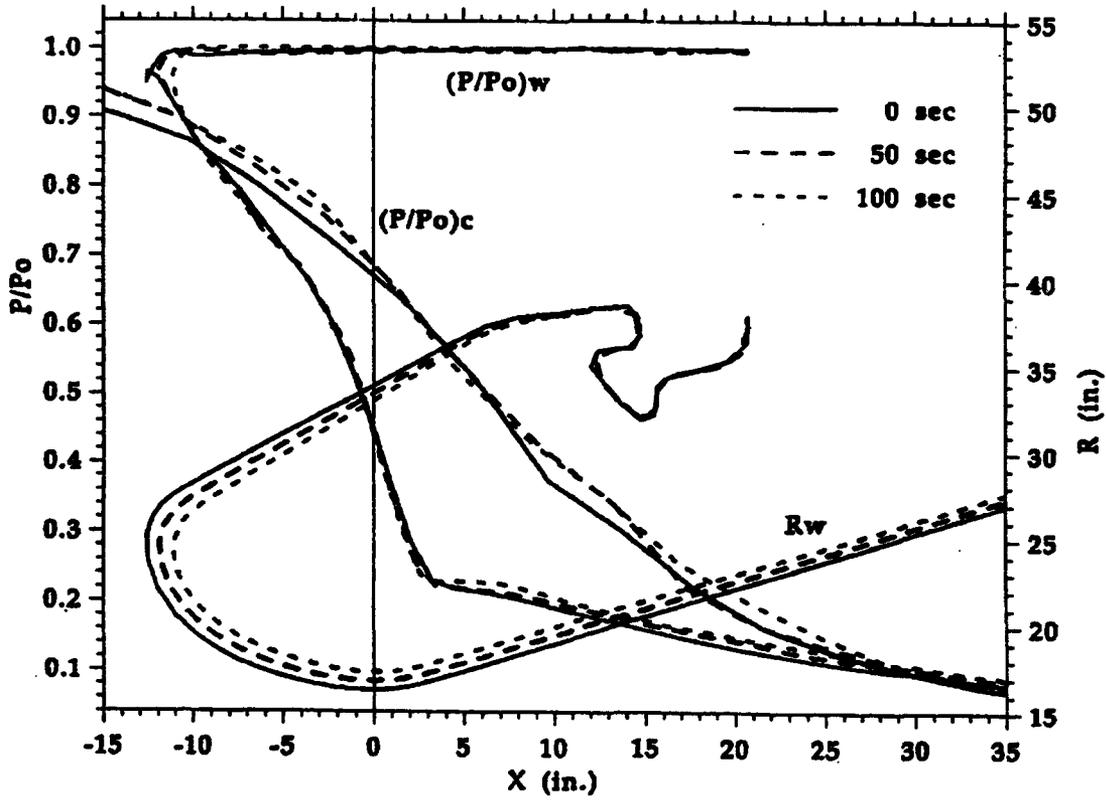
Figure 15. SRMU Nozzle Pressure Distribution

20
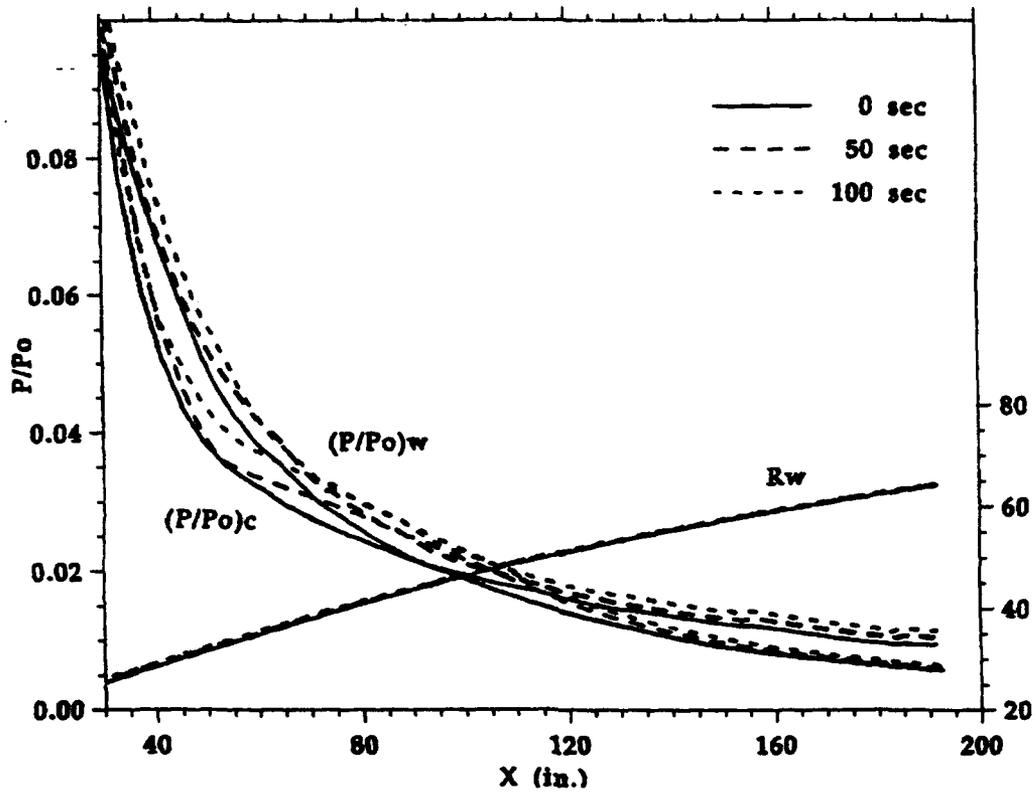
Figure 16. SRMU Exit Cone Pressure Distribution

6. THE STAR-48 MOTOR

The Star-48 motor (Ref. 11) is an upper-stage motor, which provides the impulse to propel a spacecraft (up to 2800 lb) from a low earth orbit into a geosynchronous transfer orbit. The motor has propellant loading up to 4400 lb. The motor case is made of titanium and is internally insulated with silica-filled ethylene propylene diene monomer (EPDM). The nozzle is made of three-directional carbon/carbon, and the exit cone can have either a two-directional carbon/carbon or a carbon/phenolic liner. The motor assembly and the initial grain geometry are shown in Figure 17. The chamber pressure history for a low-temperature (30°F), long-burn (94 sec) firing is given in Figure 18.

For this complicated initial grain and submerged nozzle geometry, the auxiliary program developed under this study intelligently determines the propellant burn-backs, ablated motor case insulation, and eroded nozzle-exit cone configurations at any number of time slices. These configurations, which are shown in Figure 19 at 0, 20, 40, 60, and 80 sec after ignition, are utilized directly as the computational boundaries for the mesh generation and, subsequently, for the flow-field solution. The actual ablation and erosion data from the post-fire measurement of full-scale static motors in a qualification program (Ref. 11) are used in the auxiliary program for determining the computational boundaries. The propellant burn-rate is a function of pressure ($0.0355 \cdot P^{0.30}$). For this Star-48 motor, the inlet boundaries lie on the propellant burning surfaces, and the program automatically provides the inlet flow conditions at any specified time slice.

Figure 20 depicts the basic mesh, remesh, and computed Mach number contours for the initial motor configuration. The total number of elements is 6438 for the basic mesh and 3503 for the remesh. These include 10 stretched, structured elements covering the thickness of the viscous layer, which envelops the nozzle-exit cone wall. Figure 21 gives the same information at 80 sec into the motor firing. The total number of elements is 8035 for the basic mesh and 4854 for the remesh. For the Star-48 flow-fields calculation, the ratio of specific heats is 1.150, the Prandtl number is 0.57, and the power law viscosity-temperature relationship has an exponent $A = 0.67$ and reference chamber viscosity $1.382 \cdot 10^{-8}$ lbf-sec/in.^{2} at temperature 6364°R.

The Mach number and pressure distributions are given in Figures 22 and 23, respectively. For a viscous analysis, the Mach number at the wall is zero. The "Mw" in Figure 22 representing the gas Mach number at the edge of the boundary layer is evaluated from an isentropic relation at the local wall pressure. At 0 sec, the Mach number at the exit plane of the exit cone is 3.91 at the wall and 4.11 at the centerline. The computed ratio of the static-to-chamber pressure at the exit plane of the exit cone is 0.29% at the wall and 0.14% at the centerline. At 80 sec, the Mach number at the exit plane of the exit cone is 3.85 at the wall and 4.01 at the centerline. The computed ratio of static-to-chamber pressure at the exit plane of the exit cone is 0.34% at the wall and 0.20% at the centerline. At 80 sec after ignition, the computed pressure and Mach number distributions near the throat are not smooth, which reflects the effect of the unevenly eroded nozzle wall on the flow behavior in that region. The change in nozzle surface configuration from 0 to 80 sec affects the Mach number distribution and pressure load on the wall. On the backside of the submerged nozzle, the pressure remains essentially constant at the chamber condition.

23
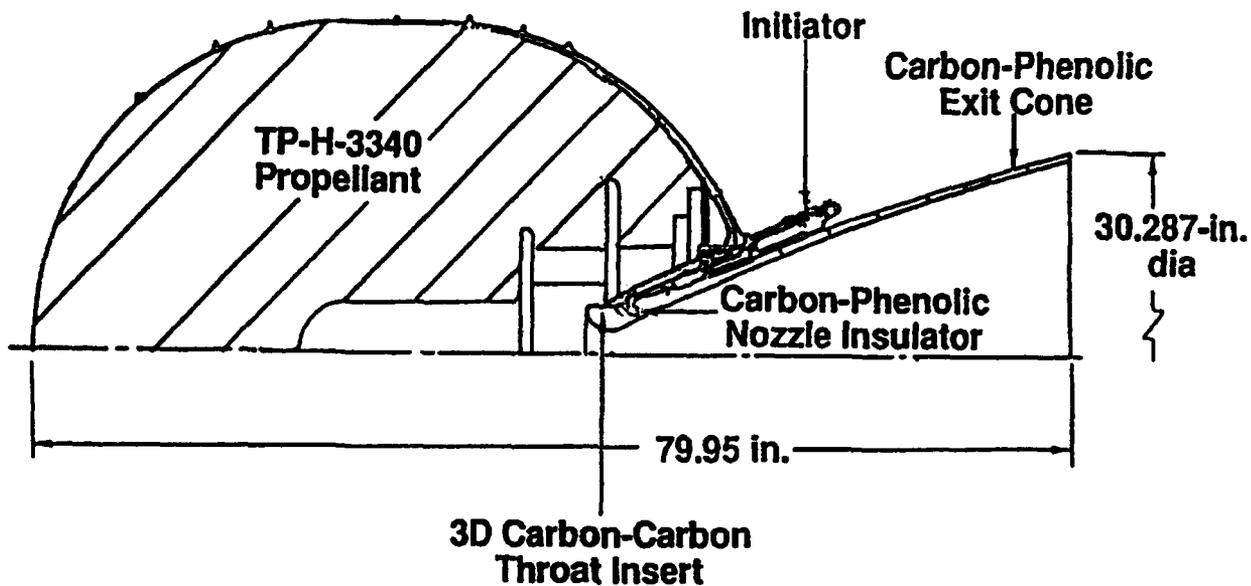
Figure 17. Star-48 Motor Assembly
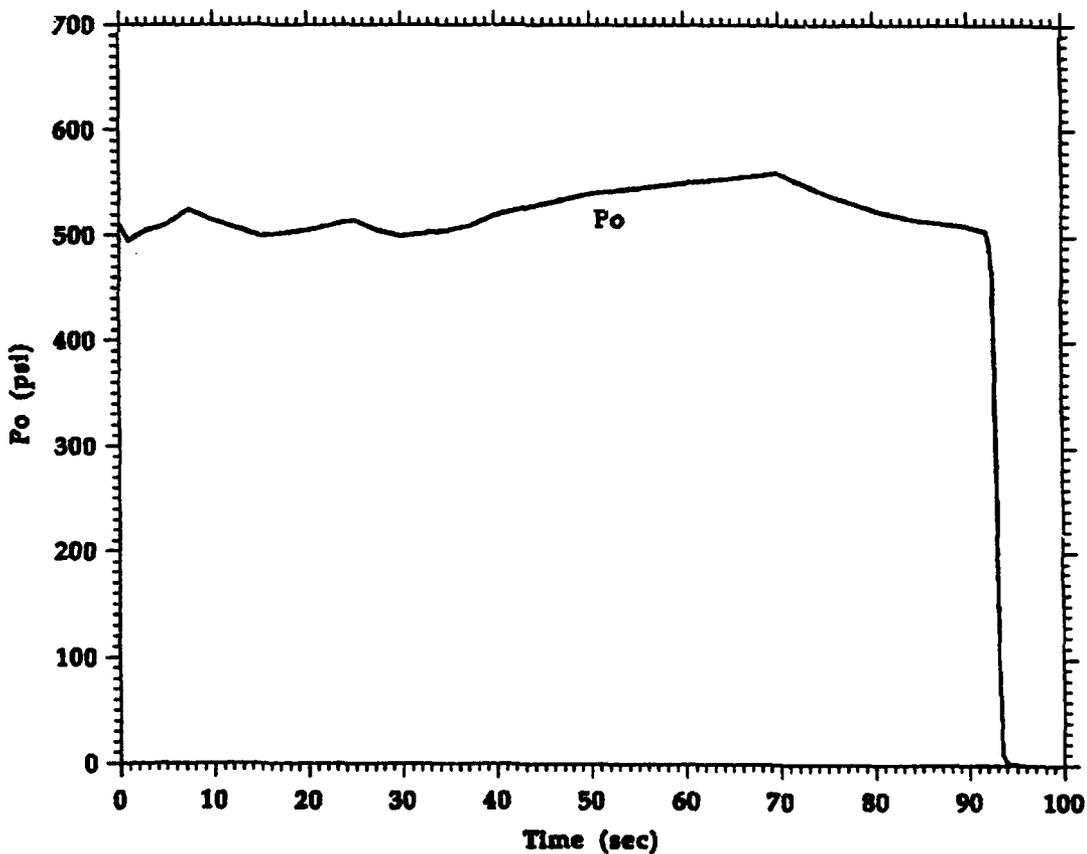
Figure 18. Star-48 Chamber Pressure History
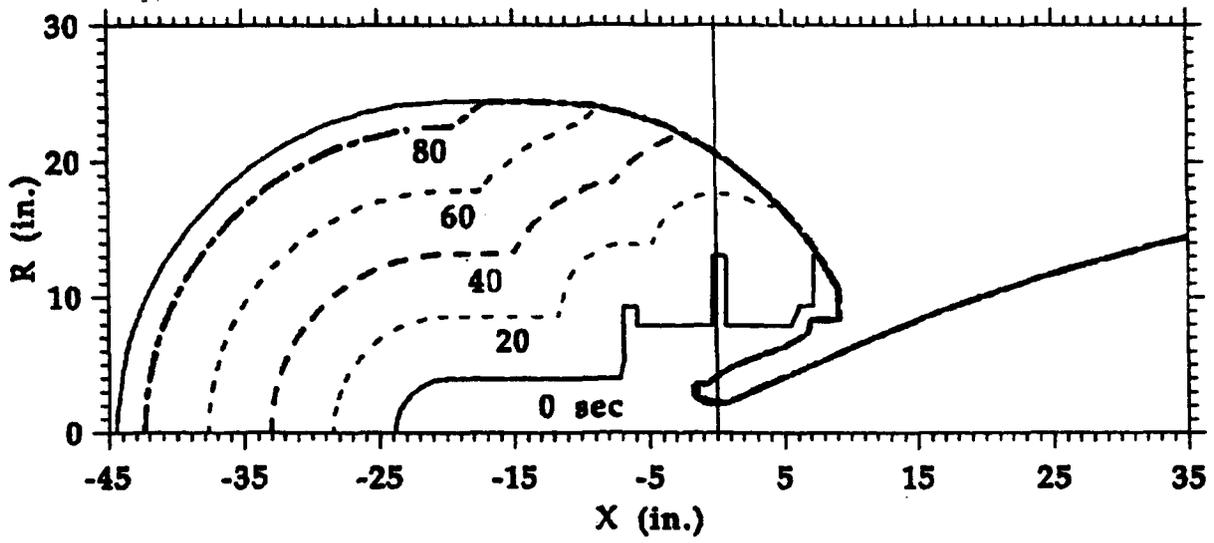
Figure 19. Star–48 Motor Configuration
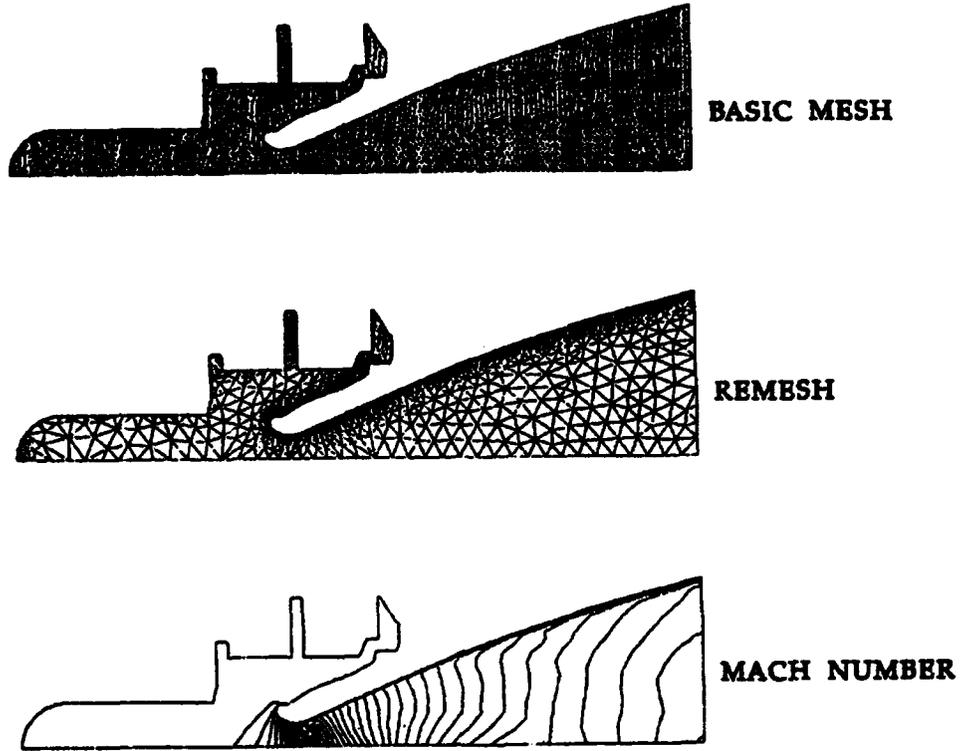
Figure 20. Star–48 Meshes and Mach Number at 0 sec

25
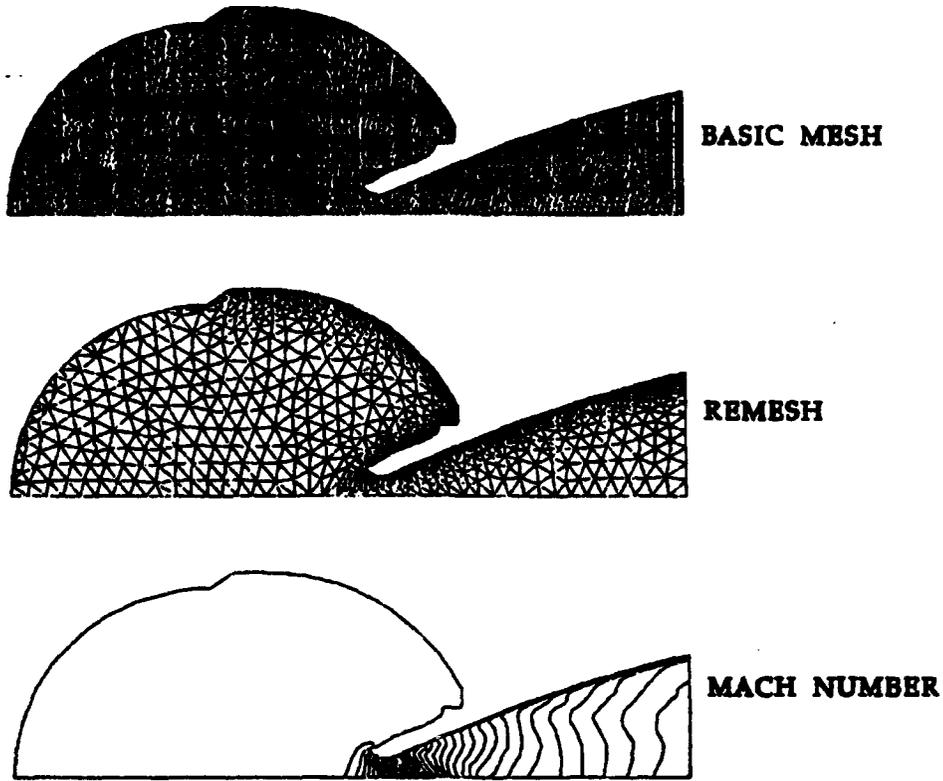
Figure 21. Star–48 Meshes and Mach Number at 80 sec
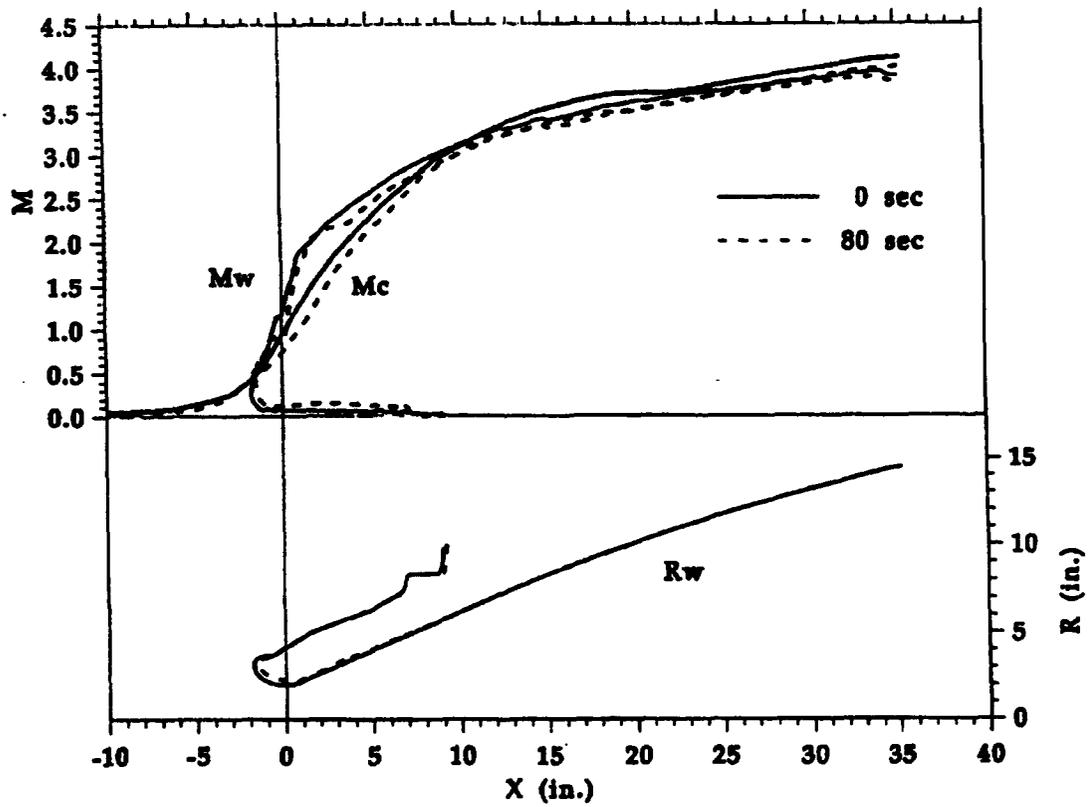
Figure 22. Star-48 Mach Number Distribution
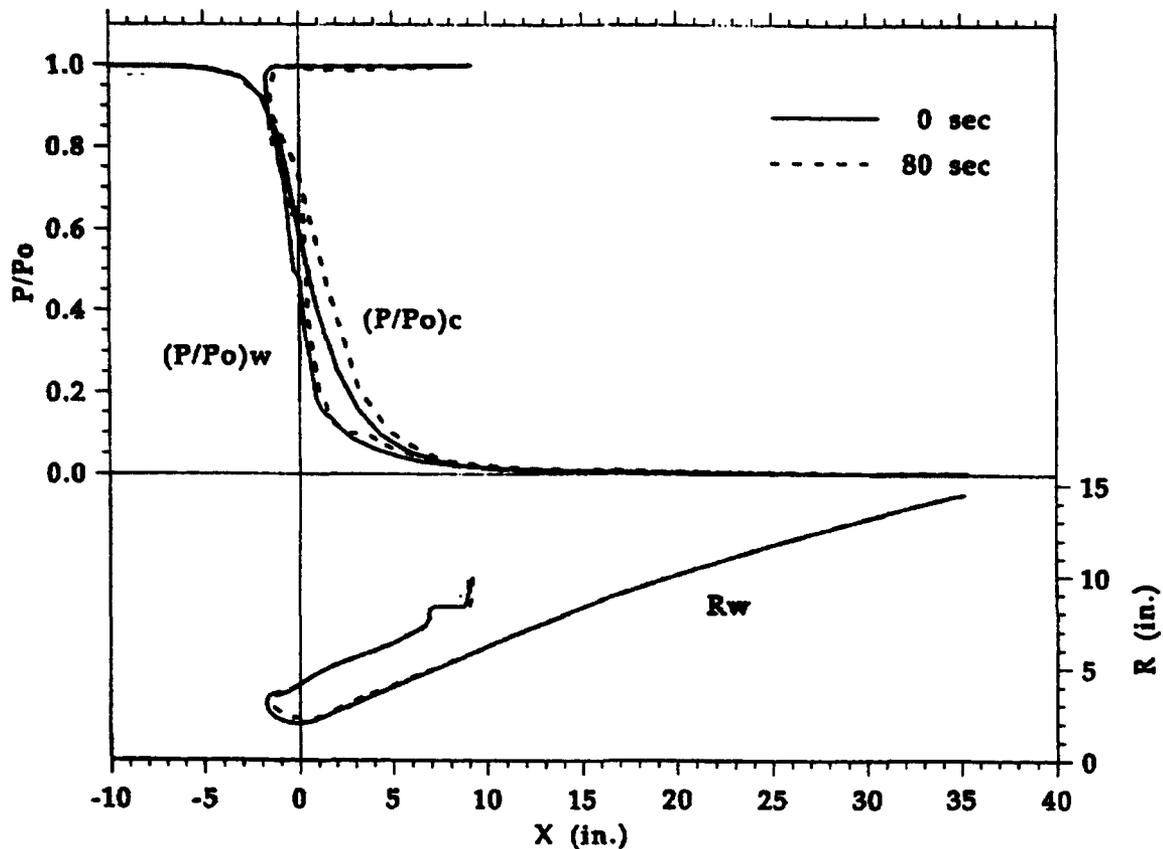
Figure 23. Star-48 Pressure Distribution

The purpose of the calculation with the Star-48 motor given here is to illustrate the capability of the adaptive, unstructured finite-element method for an efficient solution of viscous compressible flows inside a solid rocket motor with a complicated grain and nozzle configuration. A coarse mesh has been assigned in the viscous layer to prevent unnecessary consumption of the computational resource for this demonstrated calculation. Performing 500 integration steps on the basic mesh of 6438 elements takes 19 min on a Cray XMP/18 supercomputer. Performing 500 integration steps on the remesh of 3503 elements takes 11 min on the same computer. Note that remeshing results in a significant reduction in the total number of elements required to adequately cover the entire physical domain and in the amount of computation time. A meaningful flow-field solution can be obtained after approximately 2000 integration steps on the remesh. Since the Star-48 is a spinning rocket motor, final analysis based on the technique developed in this study requires a fine mesh in a viscous layer and consideration of the particle-phase subject to radial and axial acceleration in the flow field.

7. CONCLUSION

An efficient method has been developed for the solution of axisymmetric compressible viscous flows inside solid rocket motors of arbitrary geometry. A gas-particle, two-phase viscous flow analysis, similar to that given in References 6, 12, and 13 for an inviscid flow, will be the subject of study in the coming months. Further study will be directed toward the solution of a gas-particle, two-phase viscous flow with radial acceleration (spinning rocket motor) and axial acceleration (flight motor) body force terms in the governing equations. Adaptive, unstructured finite-element methods for three-dimensional flow analyses have been reported in the literature (Refs. 14 and 15). A similar technique for a three-dimensional canted or gimbaled nozzle with consideration of turbulent flow modeling also is a subject of future study.

REFERENCES

1. Peraire, J., et al., "Adaptive Remeshing for Compressible Flow Computations," *J. of Comp. Physics*, 72, 1987, pp. 449-466.

2. Thareja, R. R., et al., "A Point Implicit Unstructured Grid Solver for the Euler and Navier-Stokes Equations," AIAA paper 88-0036.

3. Stewart, J. R., et al., "Application of Finite-Element and Remeshing Technique to Shock Interference on a Cylindrical Leading Edge," AIAA paper 88-0368.

4. Serra, R. A., "Determination of Internal Gas Flows by a Transient Numerical Technique," *AIAA Journal*, 10, May 1972, pp. 603-611.

5. Ekaterinaris, J. A., N. L. Sankar, and D. P. Giddens, "Low Mach Number Compressible Flow Solutions in Constricted Ducts," AIAA paper 87-1174, AIAA 8th Computational Fluid Dynamics Conference.

6. Chang, I-Shih, "One- and Two-Phase Nozzle Flows," *AIAA Journal*, 18 (12), December 1980, pp.1455-1461; also AIAA paper 80-0272.

7. Löhner, R., J. Baum, E. Loth, and E. R. Ramamurti, "A Finite-Element Solver for Axisymmetric Compressible Flows," AIAA paper 89-1794.

8. Cuffel, R. F., L. H. Back, and P. F. Massier, "Transonic Flowfield in a Supersonic Nozzle with Small Throat Radius of Curvature," *AIAA Journal*, 7 (7), July 1969, pp. 1364-1366.

9. Back, L. H., R. F. Cuffel, and P. F. Massier, "Laminarization of a Turbulent Boundary Layer in Nozzle Flow—Boundary Layer and Heat Transfer Measurement with Wall Cooling," *ASME J. of Heat Transfer*, August 1970, pp. 333-344.

10. "Titan IV SRMU Preliminary Design Review," Hercules, Inc., February 1989.

11. "Interim Report, Star-48 Qualification Program, Volume I, Technical Discussion and Appendixes A–G," Thiokol/Elkton Division, E98-81, 9 October 1981.

12. Chang, I-Shih, "Three-Dimensional, Two-Phase, Supersonic Nozzle Flows," *AIAA Journal*, 21 (5), May 1983, pp. 671-678; also AIAA paper 81-1219.

13. Chang, I-Shih, "Three-Dimensional, Two-Phase, Transonic, Canted Nozzle Flows," *AIAA Journal*, 28 (5), May 1990, pp. 790-797; also AIAA paper 88-3201.

14. Peraire, J., et al., "Finite-Element Euler Computations in Three Dimensions," AIAA paper 88-0032.

15. Thareja, R. R., et al., "A Three-Dimensional Upwind Finite-Element Point Implicit Unstructured Grid Euler Solver," AIAA paper 89-0658.